



Atomic Pd-promoted ZnZrO_x solid solution catalyst for CO₂ hydrogenation to methanol

Kyungho Lee^{a,1}, Uzma Anjum^{a,1}, Thaylan Pinheiro Araújo^b, Cecilia Mondelli^b, Qian He^c, Shinya Furukawa^{d,e}, Javier Pérez-Ramírez^{b,*}, Sergey M. Kozlov^{a,*}, Ning Yan^{a,*}

^a Department of Chemical and Biomolecular Engineering, National University of Singapore, 4 Engineering Drive 4, Singapore 117585, Singapore

^b Institute for Chemical and Bioengineering, Department of Chemistry and Applied Biosciences, ETH Zurich, Vladimir-Prelog-Weg 1, 8093 Zürich, Switzerland

^c Department of Materials Science and Engineering, National University of Singapore, 9 Engineering Drive 1, Singapore 117575, Singapore

^d Institute for Catalysis, Hokkaido University, N-21, W-10, Sapporo 001-0021, Japan

^e Elements Strategy Initiative for Catalysis and Battery, Kyoto University, Kyoto Daigaku Katsura, Nishikyō-ku, Kyoto 615-8510, Japan

ARTICLE INFO

Keywords:

CO₂ hydrogenation

Methanol synthesis

ZnZrO_x

Palladium promoter

Atomic dispersion

ABSTRACT

The development of efficient CO₂ conversion catalysts is a long-lasting desire. Herein, we introduce an atomic Pd-promoted ZnZrO_x solid solution catalyst (Pd-ZnZrO_x), which shows markedly enhanced rate of methanol production compared to bare ZnZrO_x, as well as excellent stability over 100 h on stream. Up to 0.8 at% (*i.e.* 0.6 wt%), Pd can be atomically dispersed in ZnZrO_x, leading to more oxygen vacancies on the mixed oxide that foster methanol production. Kinetic analysis and *in situ* DRIFTS reveal that hydrogen activation is limited on ZnZrO_x, but Pd doping facilitates H₂ dissociation as well as the consequent formation of HCOO*, thus boosting CO₂ conversion to methanol. DFT analyses suggest that the presence of atomic Pd enables a more exothermic H₂ dissociation, which increases the availability of surface H and facilitates CO₂ hydrogenation on adjacent Zn sites, providing rationale on the high activity and robustness of Pd-ZnZrO_x in CO₂ hydrogenation.

1. Introduction

Taking steps forward to a circular carbon economy is a prominent global agenda. Anthropogenic CO₂ emissions have been identified as a major cause of climate change and ocean acidification [1,2]. Paradoxically, CO₂ can also be regarded as an abundant and sustainable carbon source when coupled to an efficient transformation technology. CO₂ hydrogenation to methanol has received a lot of attention because methanol is a useful platform chemical in the petrochemical industry, as well as its potential as an energy carrier in a broad range of applications [3,4]. For these reasons, various CO₂ valorization routes relying on methanol as a key intermediate are being widely explored [5–11].

CO₂ hydrogenation to methanol is thermodynamically favored at low temperature and high pressure [12]. However, since exceedingly low temperature limits the reaction kinetics, high pressure (>5 MPa) and moderate temperature (473–573 K) conditions are typically required [12,13]. Cu/ZnO/Al₂O₃ catalyst, commercially used for methanol synthesis from syngas, has been widely studied for CO₂ conversion to methanol, however, a rapid and permanent deactivation

through sintering of Cu, or segregation of Cu and ZnO species has been pointed out as a major drawback [14–16]. It is thus desirable to develop more efficient catalytic systems that simultaneously satisfy high methanol productivity and long-term stability.

Encouragingly, several oxide-based catalysts such as In₂O₃-based oxides [17–25] and MZrO_x solid solutions (*M* = Zn, Cd, Ga, *etc.*) [26–31] have been identified as promising catalysts owing to their superior methanol selectivity and lifetime. Nonetheless, metal oxide catalysts show relatively poor activity compared to Cu/ZnO/Al₂O₃ (which generally contains >60 wt% Cu), supposedly due to their inferior H₂ activation ability. Earlier literature indeed hints that the hydrogenation step over oxide-based catalysts is rate-determining. For example, Frei *et al.* observed that the reaction order of H₂ (0.3–0.5) is much larger than that of CO₂ (–0.1 to 0) for In₂O₃-based catalysts [20]. More recently, numerous reports demonstrated that metal promoters (*e.g.* Pt, Pd, Rh, Ru, Ir, Ni, Au, *etc.*) on oxide catalyst (especially In₂O₃) could substantially improve methanol yield [32–48]. A highly dispersed metal promoter can maximize the metal–oxide and/or metal–metal interfaces as well as provide a stronger H₂ splitting capability, accelerating methanol

* Corresponding authors.

E-mail addresses: jpr@chem.ethz.ch (J. Pérez-Ramírez), cheserg@nus.edu.sg (S.M. Kozlov), ning.yan@nus.edu.sg (N. Yan).

¹ These authors contributed equally

production.

In particular, for ZnZrO_x , Xu et al. showed that a small amount of Cu, Pt, and Pd can improve the methanol yield significantly [49]. The highly dispersed metal species possibly increase the hydrogenation capability through hydrogen spillover. More recently, Huang et al. reported Pd-doped ZnZrO_x to promote methanol yield [50]. In contrast with Xu's hypothesis, the proposed Pd promoting effect is not critically related to faster H_2 dissociation, but to the creation of a higher density of oxygen vacancies, which facilitate CO_2 adsorption and activation. Thus, a deeper understanding of how metal doping tunes the catalyst structure and changes the reaction mechanism is required to uncover the full potential of metal promoters on the activity of ZnZrO_x catalysts.

Prepared by coprecipitation, herein we introduce a novel Pd- ZnZrO_x solid solution catalyst featuring atomically dispersed palladium species onto ZnZrO_x . The atomic Pd-doping markedly enhances the methanol production activity and is accompanied by excellent long-term stability, which is attractive towards large-scale CO_2 valorization. Comprehensive experimental and computational analyses indicate that the atomic Pd dopant increases the number of surface oxygen vacancies which is responsible for CO_2 activation, and accelerates the formation of key hydrogenated intermediates (e.g. HCOO^*), thereby promoting the overall CO_2 hydrogenation activity.

2. Experimental section

2.1. Materials

$\text{Zn}(\text{NO}_3)_2 \cdot 6\text{H}_2\text{O}$ (98%), $\text{ZrO}(\text{NO}_3)_2 \cdot x\text{H}_2\text{O}$ (99%), $\text{Pd}(\text{NO}_3)_2 \cdot x\text{H}_2\text{O}$ (40% Pd basis), and $(\text{NH}_4)_2\text{CO}_3$ ($\geq 30\%$ NH_3 basis) were purchased from Sigma Aldrich and were used without further treatment.

2.2. Catalyst preparation

The ZnZrO_x ($\text{Zr}/\text{Zn} = 5$) catalyst was prepared by a coprecipitation method. Typically, 1.325 g of $\text{Zn}(\text{NO}_3)_2 \cdot 6\text{H}_2\text{O}$ and 5.66 g of $\text{ZrO}(\text{NO}_3)_2 \cdot x\text{H}_2\text{O}$ were dissolved in 70 cm^3 of deionized (DI) water at 343 K. The precipitant 0.625 M $(\text{NH}_4)_2\text{CO}_3$ aqueous solution 50 cm^3 was added dropwise to the aforementioned solution under vigorous stirring to obtain pH 7. The suspension was aged for 2 h at 343 K, followed by cooling down to room temperature. Then, the precipitate was recovered by centrifugation (10,000 rpm, 2 min) and washed thoroughly with DI water. The resulting gel was dried at 373 K for 8 h and calcined at 773 K under air flow for 3 h. Finally, the calcined sample was reduced at 673 K under 0.1 MPa H_2 flow for 2 h. Pd-incorporated ZnZrO_x catalysts ($n\%$ Pd- ZnZrO_x , $n = 0.2, 0.4, 0.8, 1.5$ at% among metal elements) were prepared following the same coprecipitation method as for ZnZrO_x while adding $\text{Pd}(\text{NO}_3)_2 \cdot x\text{H}_2\text{O}$ into the Zn and Zr precursors solution before precipitation. Samples reported here indicate a reduced state at 673 K unless otherwise specified. The synthesis procedure of ZnO , Pd-ZnO , ZrO_2 , Pd-ZrO_2 , and Pd-ZnZrO_x catalysts from other precursors is described in the Supporting Information (SI).

2.3. Catalyst characterization

The catalysts were characterized by a series of techniques. Instrument and analysis details for elemental analysis by inductively coupled plasma-optical emission spectroscopy (ICP-OES), temperature programmed reduction (H_2 -TPR), X-ray absorption spectroscopy (XAS), transmission electron microscopy (TEM) and high angle annular dark field scanning transmission electron microscopy (HAADF-STEM), X-ray diffraction (XRD), X-ray photoelectron spectroscopy (XPS), electron paramagnetic resonance spectroscopy (EPR), N_2 physisorption, and CO_2 -temperature programmed desorption (CO_2 -TPD) are described in the SI.

2.4. Catalyst evaluation

All reactions were carried out in a continuous-flow fixed-bed reactor. CO_2 hydrogenation was conducted under conditions of 473–673 K, 5 MPa, $\text{CO}_2/\text{H}_2/\text{Ar} = 19:76:5$, $\text{GHSV} = 24,000 \text{ cm}^3 \text{ g}_{\text{cat}}^{-1} \text{ h}^{-1}$. The detailed procedure is described in the SI. Reported data are given as values of time-on-stream at 3 h, unless otherwise stated. For kinetic analyses, tests were carried out at a low CO_2 conversion ($<6\%$) in order to avoid thermodynamic limitations. Apparent activation energies were determined by the results acquired at 473–553 K. The reaction order of CO_2 was determined at 533 K, $\text{GHSV} = 24,000 \text{ cm}^3 \text{ g}_{\text{cat}}^{-1} \text{ h}^{-1}$ by controlling the partial pressure of CO_2 (P_{CO_2}) from 0.5 MPa to 0.95 MPa under a fixed partial pressure of H_2 (P_{H_2} , 3.8 MPa), and the reaction order of H_2 was attained similarly, by controlling P_{H_2} from 2.6 MPa to 4.1 MPa under a fixed P_{CO_2} of 0.65 MPa. The total pressure of reactant gas mixture was kept at 5 MPa by using Ar as balance gas as well as internal standard. The equilibrium yield of methanol was calculated using Outotec HSC software. CO hydrogenation was conducted similarly under conditions of 493–593 K, 5 MPa, $\text{CO}/\text{H}_2/\text{Ar} = 19:76:5$, $\text{GHSV} = 24,000 \text{ cm}^3 \text{ g}_{\text{cat}}^{-1} \text{ h}^{-1}$.

2.5. In situ DRIFTS

In situ diffuse reflectance infrared Fourier transform spectroscopy (DRIFTS) was carried out during CO_2 hydrogenation at 0.1 MPa using a Nicolet iS50 spectrometer (Thermo Fisher) and a Pike Diffuse IR chamber with ZnSe windows. For each analysis, ca. 50 mg of catalyst was placed into the chamber, and pre-treated under H_2 flow (40 $\text{cm}^3 \text{ min}^{-1}$) at 673 K for 2 h, followed by N_2 flow at the same temperature for 4 h to make a clean catalyst surface. Then, the sample was cooled down to a target temperature (373, 423, 473, 523, and 573 K) under N_2 flow. After reaching a target temperature, a background was recorded, followed by admission of a CO_2/H_2 mixture (1/4 ratio, 40 $\text{cm}^3 \text{ min}^{-1}$) to the chamber. Spectra were recorded after 90 min of equilibration time. The time-dependent spectra under CO_2/H_2 flow and H_2 flow were measured by recording spectra every 1 min at 523 K. To obtain D_2 -adsorbed spectra, catalysts were pre-treated similarly as mentioned above. After cooling down, background was recorded at 323 K under N_2 flow, and then D_2 flow (40 $\text{cm}^3 \text{ min}^{-1}$) was dosed to the chamber. Spectra were collected after 30 min D_2 flow.

2.6. Computational details

To simulate Pd- ZnZrO_x and ZnZrO_x systems and to calculate the mechanistic properties for CO_2 hydrogenation reactions, spin-polarized Density Functional Theory (DFT) simulations were performed using the Vienna *Ab initio* Simulation Package (VASP) software [51]. PBE exchange-correlation functional and projected augmented wave (PAW) method [52] to treat core electrons were utilized for all calculations. A plane-wave basis set with a cut-off of 400 eV energy was employed for the calculations. A (101) slab of three ZrO_x layers of (2×2) surface areas with a supercell dimension of 12.82 Å and 7.29 Å was constructed with a vacuum of 15 Å. One bottom ZrO_x layer was fixed to the bulk geometry and two top ZrO_x were relaxed in the procedure. $2 \times 3 \times 1$ Monkhorst-Pack k-point mesh [53] and Gaussian smearing with width of 0.1 eV were employed for all the slab calculations. The ZnZrO_x model structure was constructed by substituting one Zr atom from the surface with one Zn atom. Similarly, in the Pd- ZnZrO_x model, one Zn and one Pd atom substituted two surface Zr atoms. Ionic relaxation was converged to 0.02 eV/Å force criteria using conjugate gradient algorithm with an SCF accuracy of 10^{-5} eV. The Gibbs energy for oxygen vacancy generation ($G_{\text{O-vac}}$) on the surface of Pd- ZnZrO_x and ZnZrO_x was calculated as,

$$G_{\text{O-vac}} = G(\text{O-vac/slab}) - G(\text{slab}) + G(\text{H}_2\text{O}) - G(\text{H}_2) \quad (1)$$

where $G(\text{O-vac/slab})$ and $G(\text{slab})$ are the Gibbs energies for the catalyst

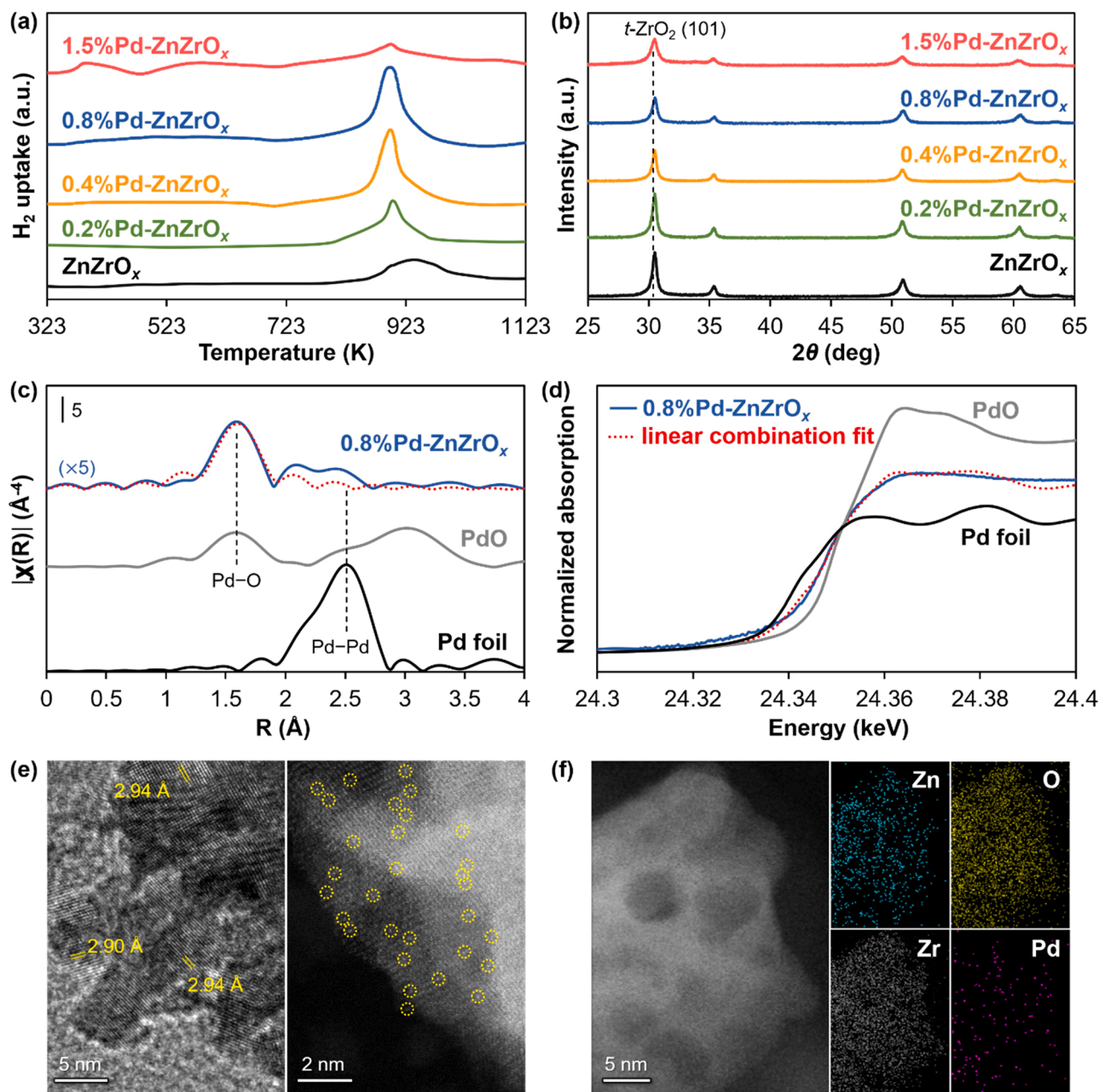


Fig. 1. (a) H₂-TPR profiles of calcined ZnZrO_x and Pd-ZnZrO_x. (b) Powder XRD patterns of ZnZrO_x and Pd-ZnZrO_x catalysts. (c) Pd K edge k^3 -weighted Fourier transforms of the EXAFS, and (d) XANES of the 0.8%Pd-ZnZrO_x catalyst. (e) TEM and HAADF-STEM images, and (f) EDX elemental maps of the 0.8%Pd-ZnZrO_x catalyst.

surface with and without oxygen vacancy, while $G(\text{H}_2\text{O})$ and $G(\text{H}_2)$ are the Gibbs energies of gas-phase H₂O and H₂ molecules, respectively.

The total energies of gas-phase H₂O, H₂, and CO₂ species were calculated in a box of $10 \text{ \AA} \times 10 \text{ \AA} \times 10 \text{ \AA}$ size at Γ -point in Brillouin zone. Gibbs energy calculations were implemented using ideal gas and harmonic approximation for gas phase and adsorbed species, respectively, at 573 K and partial pressures of 4, 0.65, and 0.1 MPa for H₂, CO₂, and H₂O, respectively, using the atomic simulation environment [54]. Vibrational frequency analysis was performed using finite displacements of 0.02 Å.

3. Results and discussion

3.1. Structure of Pd-ZnZrO_x

A series of Pd-containing ZnZrO_x (Pd-ZnZrO_x) catalysts were prepared by coprecipitation method while keeping the molar Zr/Zn ratio at 5. The catalysts were calcined at 773 K in air and reduced at 673 K in H₂ before catalytic tests. The Pd-ZnZrO_x and reference ZnZrO_x catalysts were characterized to elucidate their composition and structure. Elemental analysis using ICP-OES confirmed that the Pd content in the catalysts was 0.18, 0.28, 0.62, and 1.12 wt% for 0.2, 0.4, 0.8, and 1.5 at % Pd-doping, respectively. The molar Zr/Zn ratio was 4.66–4.95 for all samples, in good agreement with the nominal value (Table S1).

Temperature-programmed reduction using hydrogen (H₂-TPR) of the calcined Pd-ZnZrO_x catalysts with different Pd content is depicted in

Fig. 1a. For a better understanding, the TPR patterns of ZnO, ZrO₂, Pd-ZnO, and Pd-ZrO₂ (0.8 at% Pd loaded) prepared by a similar (co)precipitation method are shown in Fig. S1a. The profile of bare ZnZrO_x shows a single reduction peak at 930 K, which is in between the reduction peak of pure ZnO and ZrO₂, indicating that the two metal oxide components (ZnO and ZrO₂) are well mixed. Until 0.8 at% Pd loading, all Pd-ZnZrO_x catalysts also show a single reduction peak at a slightly lower temperature (900 K), which similarly suggest that the Pd species are uniformly dispersed in ZnZrO_x. At a high Pd loading (1.5 at %), the reduction peak at 900 K decreases, while new broad peaks at lower temperatures (~390 and ~560 K) appear simultaneously. These changes indicate that high palladium loadings significantly alter the chemical properties of ZnZrO_x and evidence the heterogeneity of the catalyst at high Pd loading, such as the presence of loosely supported Pd nanoparticles and/or the formation of PdZn alloy that are confirmed by H₂-TPR analysis of Pd-ZnO and Pd-ZrO₂.

Powder X-ray diffraction (XRD) patterns of ZnZrO_x and Pd-ZnZrO_x catalysts are represented in Fig. 1b. In all catalysts, only the characteristic peaks for *tetragonal*-ZrO₂ (*t*-ZrO₂) were detected. The enlarged patterns around $2\theta = 36\text{--}43^\circ$ confirm the absence of large crystalline Pd, PdZr, and PdZn domains (Fig. S2a). It should be noted that the presence of PdZn intermetallic alloy in reduced 0.8%Pd-ZnO was clearly confirmed in XRD when a similar amount of Pd (0.8 at%) was loaded onto ZnO (Fig. S1b). Up to 1.5 at% Pd loading, ZnZrO_x-based catalysts have the same diffraction angle, indicating similar lattice parameters. The diffraction peak intensity gets smaller along with increased Pd loading which implies Pd incorporation leads to a more defective structure (Fig. S2b).

The extended X-ray absorption fine structure (EXAFS) function of the 0.8%Pd-ZnZrO_x after reduction at 673 K shows a dominant contribution of the Pd-O scattering (Fig. 1c). Meanwhile, no appreciable Pd-Pd contribution is observed. The EXAFS fitting results suggest that Pd is anchored by approximately two to three oxygen atoms in ZnZrO_x without Pd-Pd, Pd-Zn, and Pd-Zr bonds (Table S2). X-ray absorption near-edge structure (XANES) analysis reveals that Pd has a cationic character (ca. +1), which further supports the presence of highly dispersed, oxygen-bound isolated Pd species in ZnZrO_x (Fig. 1d).

According to microscopic analysis, ZnZrO_x has ca. 10 nm crystalline particles with interplanar spacing of 2.90–2.96 Å, which is attributed to a *t*-ZrO₂-like phase (Fig. S3). Pd-ZnZrO_x also shows only a *t*-ZrO₂-like structure, while no Pd nanoparticles (interplanar spacing: 2.0–2.2 Å) were observed (Fig. 1e). Notably, aggregated Pd nanoparticles were not detected over the entire microscopy analysis. Instead, numerous bright dots were observed (Fig. 1e, right panel). This result corroborates the presence of atomically dispersed Pd species in ZnZrO_x. EDX elemental maps show that not only Zn and Zr, but also Pd are highly dispersed in the ZnZrO_x crystal (Fig. 1f), further confirming the uniform atomic dispersion of Pd without any clustering. As a comparison, the dominant presence of PdZn species and nm-scale metallic Pd domain are clearly observed in TEM analysis of Pd-ZnO and Pd-ZrO₂, respectively (Fig. S1c and d).

Previously, Flytzani-Stephanopoulos et al. studied the structure of noble metal-doped ZnZrO_x. They found that a ZnZrO_x with homogeneous Zn dispersion (Zn:Zr = 1:10) can support atomically dispersed Au species up to 0.5 wt% in a very stable manner [55]. However, in another work from the same group, 1 wt% Pd impregnated onto ZnZrO_x formed a PdZn alloy which strongly interacted with Zn and Zr species rather than existing as isolated atomic Pd species [56]. Notably, ZnZrO_x in this work was not a solid solution but was composed of mixed hexagonal-ZnO and *t*-ZrO₂ phases, presumably due to the high Zn content (Zn:Zr = 1:1). This feature implies that compositional and structural features of ZnZrO_x greatly affect the state of metal dopants. As we discussed, unlike the pure ZnO and ZrO₂, ZnZrO_x can allow atomic Pd dispersion upto an incredibly huge loading (ca. 0.8 at%, in other words, 0.6 wt%). Thus, the strong anchoring effect for atomic Pd species is a unique feature of the ZnZrO_x solid solution.

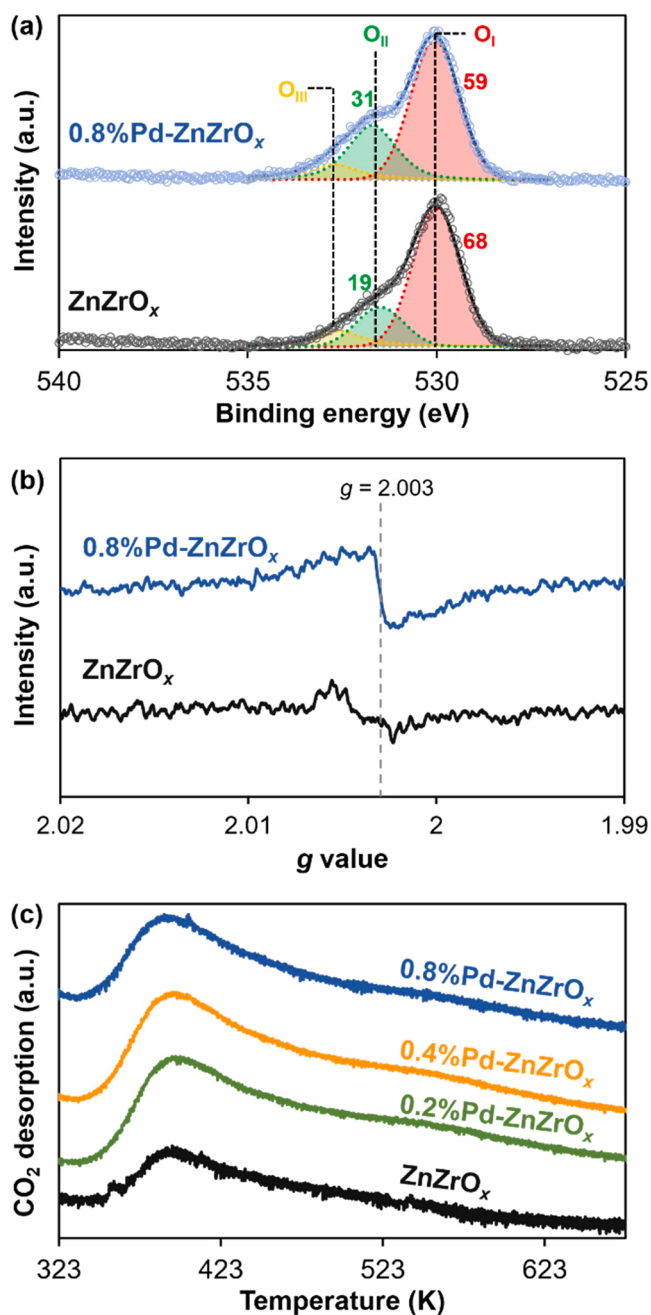


Fig. 2. (a) O1s core-level XPS and (b) EPR spectra of ZnZrO_x and 0.8%Pd-ZnZrO_x catalysts. (c) CO₂-TPD profiles of ZnZrO_x and Pd-ZnZrO_x catalysts.

To characterize the surface properties of catalysts, X-ray photoelectron spectroscopy (XPS) was carried out for ZnZrO_x and Pd-ZnZrO_x catalysts. In the Zr 3p and Pd 3d regions (Fig. S4a), two strong peaks at 333 eV and 347 eV represent Zr 3p_{3/2} and Zr 3p_{1/2} signals, respectively. Due to the high contribution of Zr and low surface concentration of Pd, Pd 3d signals were not detected clearly. XPS of Zr 3d and Zn 2p are shown in Fig. S4b–c. The binding energy of Zr and Zn in ZnZrO_x and Pd-ZnZrO_x catalysts are slightly reduced (ca. 0.2 eV) compared to that of ZrO₂ and ZnO. Nevertheless, there are no significant differences in the binding energies (≤ 0.1 eV) of both Zr and Zn species regardless of the content of Pd in ZnZrO_x-based catalysts, which indicate that Pd-doping does not considerably alter the charge of Zn and Zr in ZnZrO_x.

The O1s region was also analyzed to access information about oxygen vacancies (Fig. 2a). The O1s signal can be deconvoluted to three different oxygen species: The first one at 530.0 eV (O₁) represents the

Table 1Surface composition and gas adsorptive properties of ZnZrO_x and Pd-ZnZrO_x catalysts.

Sample	Surface conc. (%) ^a			Oxygen distribution (%)			S_{BET} (m ² g ⁻¹) ^e	n_{CO_2} (μmol m ⁻²) ^f
	Pd	Zn	Zr	O _I ^b	O _{II} ^c	O _{III} ^d		
ZnZrO _x	n.	20.7	79.3	68.3	19.0	12.7	37	16.6
0.2%Pd-ZnZrO _x	n.	21.6	78.4	61.3	29.2	9.5	46	21.2
0.4%Pd-ZnZrO _x	n.	23.3	76.7	60.0	29.1	10.9	35	22.4
0.8%Pd-ZnZrO _x	n.	20.9	79.1	59.3	31.0	9.7	41	22.8

^a The content (%) among metal elements (Pd, Zn, and Zr) measured by XPS.^b Lattice oxygen.^c Oxygen which is neighbored to a defect site (i.e., oxygen vacancy).^d Oxygen in hydroxyl groups.^e BET surface area measured by N₂ physisorption at 77 K.^f Surface area-normalized CO₂ adsorption capacity determined by CO₂-TPD and S_{BET} .^g Not detected.

lattice oxygen, the second one at 531.7 eV (O_{II}) indicates the oxygen which is neighbored to a defect site, and the last one at 532.7 eV (O_{III}) is the oxygen in surface hydroxyl groups or adsorbed from surface-adsorbed oxygen. In general, the ratio of O_{II} is widely used as a qualitative indicator for the amount of surface oxygen vacancies. As shown in Fig. 2a, Pd-doping of ZnZrO_x decreases surface lattice oxygen content (O_I) and increases defect-neighbored oxygen (O_{II}). Quantitative analysis of surface elements (Table 1) shows that the surface Zn/Zr ratio is constant (ca. 0.25) for all catalysts, but even a small amount of Pd (e.g. 0.2 at%) can significantly alter the surface oxygen distribution, indicating that addition of Pd generates a consistent surplus of surface oxygen vacancies. In EPR spectra (Fig. 2b), 0.8%Pd-ZnZrO_x shows more intense signal than ZnZrO_x at a g value of 2.003, which is attributed to unpaired electrons trapped in oxygen vacancies. [57,58] Although the EPR signal cannot tell the location of oxygen vacancies, it should be noted the formation of oxygen vacancies is thermodynamically more favored on the surface than in the bulk. [59] Together with the O1s XPS results, EPR result confirms that the atomically dispersed Pd creates more surface oxygen vacancies.

It has been reported that oxygen vacancy is indispensable for CO₂ adsorption and activation for oxide-based catalysts [17,18,23,34]. As seen from the CO₂-TPD profile (Fig. 2c), ZnZrO_x and Pd-ZnZrO_x catalysts show similar adsorption strength of CO₂. The quantification of surface area-normalized CO₂ adsorption capacity (n_{CO_2}) reveals that Pd-ZnZrO_x catalysts on average show 1.3-fold increased n_{CO_2} (21.2–22.8 μmol m⁻²) compared to that of bare ZnZrO_x (16.6 μmol m⁻²) (Table 1). This hints to a higher concentration of surface oxygen vacancies in the Pd-ZnZrO_x catalysts.

From the analysis above, Pd-ZnZrO_x catalysts prepared by coprecipitation form atomically dispersed Pd in ZnZrO_x up to relatively high loading (0.8 at%) and retain their atomic Pd dispersion even after reduction at 673 K (i.e., conventional pretreatment condition for reducing PdO). Based on these observations, we suggest that Pd substitutes surface Zn or Zr site. Atomic Pd-doping does not significantly alter textural features of ZnZrO_x in terms of particle size, crystalline phase, surface area, and surface Zn:Zr ratio. Interestingly, as Pd dopant is anchored by lattice oxygen atoms with low coordination numbers (ca. 2), it creates adjacent oxygen vacancies.

3.2. Impact of atomic Pd-doping on CO₂ hydrogenation

The CO₂ hydrogenation performances of 0.2–0.8% Pd-ZnZrO_x catalysts which contain uniform atomic Pd dispersion and bare ZnZrO_x were

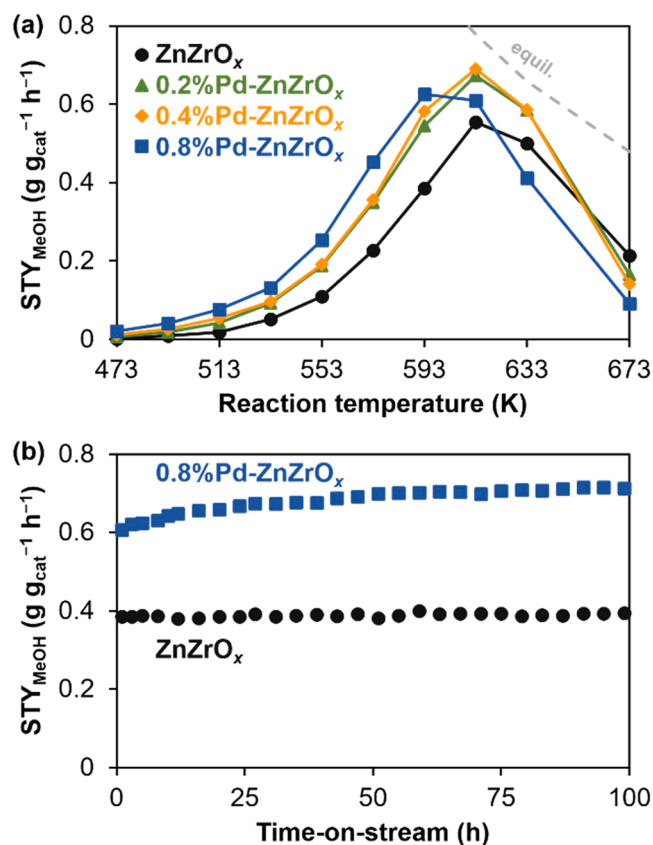


Fig. 3. (a) Space-time yield of methanol over ZnZrO_x and Pd-ZnZrO_x catalysts during CO₂ hydrogenation as a function of reaction temperatures. (b) Long-term test of ZnZrO_x and 0.8%Pd-ZnZrO_x catalysts at 593 K (Condition: 5 MPa, CO₂/H₂ = 1:4, GHSV = 24,000 cm³ g_{cat}⁻¹ h⁻¹).

tested at various temperatures at 5 MPa, CO₂/H₂/Ar = 19/76/5, and 24,000 cm³ g_{cat}⁻¹ h⁻¹. During CO₂ hydrogenation, methanol and CO were always detected as major products. Owing to the cooperation of kinetics and thermodynamics, the CO₂ conversion increased as reaction temperature increased (Fig. S5a). Meanwhile, the methanol selectivity kept constant until 593 K but rapidly decreased thereafter (Fig. S5b). As a consequence, the space-time yield of methanol (STY_{MeOH}) plot shows a volcano-shaped curve with maximum at around 593–613 K (Fig. 3a). Methanol selectivities do not change significantly in the conversion range ca. 1–20%, in particular for Pd doped catalysts (Fig. S5c). A small amount of methyl formate was detected in the very low conversion regime but its selectivity became negligible when the conversion exceeded 1%. Dimethyl ether was also detected as a side product but its selectivity never exceed 1.5%. Methyl formate and dimethyl ether are likely produced via condensation of methanol with formate species and methanol, respectively.

The pristine ZnZrO_x exhibits high methanol selectivity (>85%), however, it shows limited CO₂ conversion (<7%) below 593 K. Pd-doping enhances the CO₂ conversion greatly while decreasing the selectivity to methanol slightly (Fig. S5). As a consequence, atomic Pd-doping increases the net methanol formation rate especially under the kinetic-controlled regime (≤593 K) (Fig. 3a). In detail, the STY_{MeOH} plots are shifted to a ~20 K lower temperature region for 0.2%Pd- and 0.4%Pd-ZnZrO_x catalysts, and more than 30 K lower region in 0.8%Pd-ZnZrO_x catalyst. The maximum STY_{MeOH} for each catalyst was also enhanced greatly after Pd-doping. The Pd-free ZnZrO_x exhibits a maximum STY_{MeOH} of 0.55 g g_{cat}⁻¹ h⁻¹ at 613 K, while Pd-ZnZrO_x catalysts show a markedly enhanced maximum STY_{MeOH} of 0.63–0.69 g g_{cat}⁻¹ h⁻¹ at 593–613 K. The STY_{MeOH} is proportionally increased with respect to Pd content up to 0.8% (Fig. S6), which is

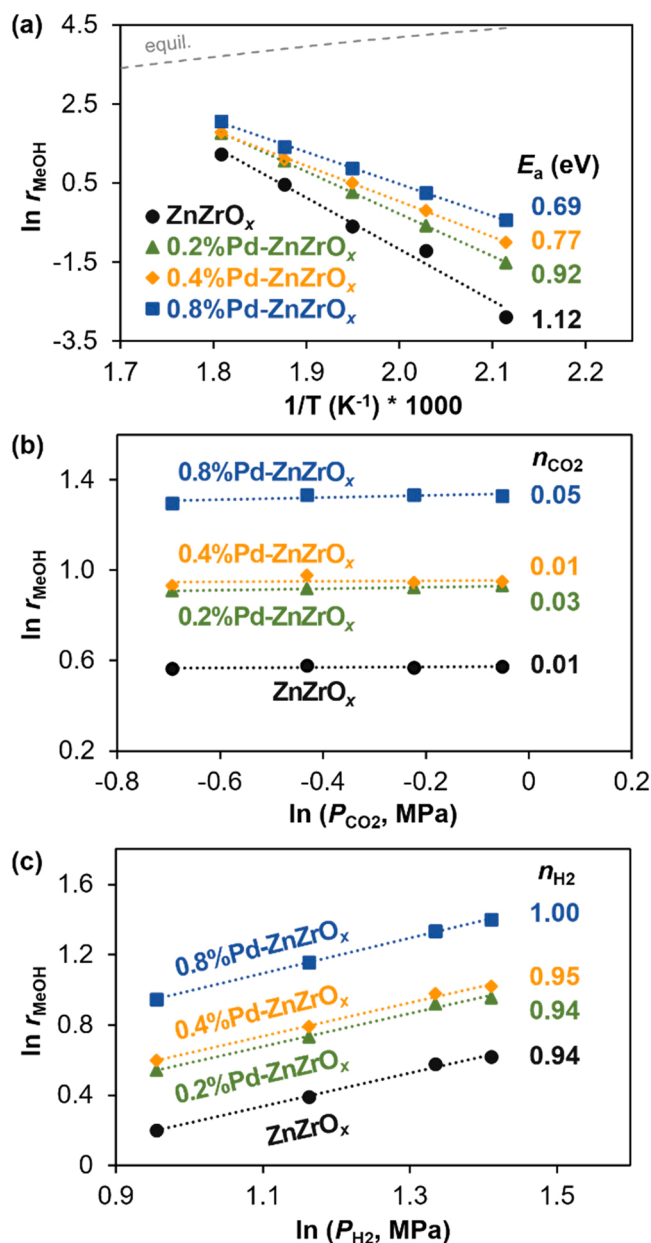


Fig. 4. (a) Arrhenius plot for apparent activation energy determination (Condition: 473–553 K, 5 MPa, $\text{CO}_2/\text{H}_2 = 1:4$, $\text{GHSV} = 24,000 \text{ cm}^3 \text{ g}_{\text{cat}}^{-1} \text{ h}^{-1}$). Reaction order analysis of (b) CO_2 and (c) H_2 for methanol formation over ZnZrO_x and Pd-ZnZrO_x catalysts (Condition: 533 K, 5 MPa, $\text{GHSV} = 24,000 \text{ cm}^3 \text{ g}_{\text{cat}}^{-1} \text{ h}^{-1}$). The unit of r_{MeOH} is $\text{mmol g}_{\text{cat}}^{-1} \text{ h}^{-1}$.

attributed to the uniform decoration of active sites by the atomically dispersed Pd.

0.8%Pd-ZnZrO_x also shows excellent long-term stability (Fig. 3b). Interestingly, STY_{MeOH} for 0.8%Pd-ZnZrO_x increased as the reaction continued, eventually reaching $0.71 \text{ g g}_{\text{cat}}^{-1} \text{ h}^{-1}$ after 100 h. During the process, the CO_2 conversion remained mostly constant, but the methanol selectivity steadily increased while suppressing CO formation (Fig. S7). This online promotion of methanol production is only observed over Pd-ZnZrO_x, but not over ZnZrO_x. To monitor the structural changes of catalyst upon reaction, we conducted XAFS, XRD, HAADF-STEM and XPS analyses of 0.8%Pd-ZnZrO_x catalyst after 100 h reaction (Figs. S8 and S9). XAFS results indicate that Pd still remains as low-coordinated cationic (ca. +1 determined by linear combination fitting from XANES) species, although the Pd–Pd coordination number slightly increased (1.5 ± 0.7). The increase of Pd–Pd coordination number can

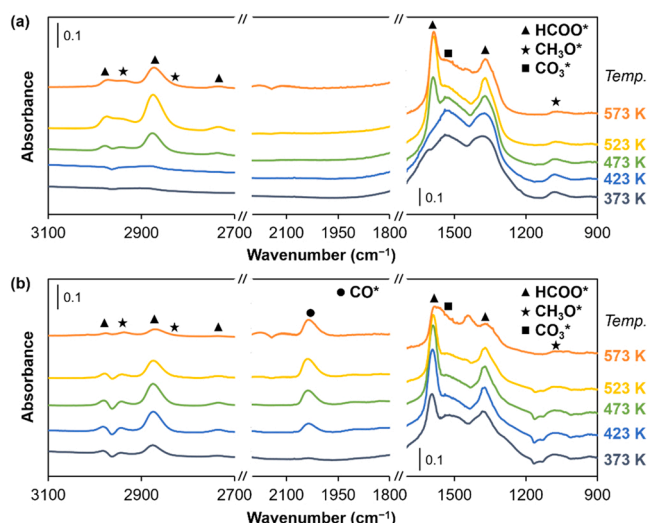


Fig. 5. Temperature-dependent *in situ* DRIFT spectra during CO_2 hydrogenation over (a) ZnZrO_x and (b) 0.8%Pd-ZnZrO_x. (Conditions: 373–573 K, 0.1 MPa, $\text{CO}_2/\text{H}_2 = 1:4$, $40 \text{ cm}^3 \text{ min}^{-1}$, and $W_{\text{cat}} = \text{ca. } 50 \text{ mg}$).

imply migration/clustering of Pd atoms during reaction, while the small coordination number indicates that the majority of Pd is still present as a highly dispersed species. XRD and HAADF-STEM analysis confirm the highly dispersed state of Pd and the well-preserved crystallinity without forming large Pd or PdZn domains. XPS analysis suggests the surface concentration of Pd is still below the detection limit. Notably, the concentration of the surface oxygen vacancy has increased during reaction, which might be the reason for the increased methanol yield.

To understand the nature of the promoting effect of atomically dispersed Pd, the kinetics of CO_2 hydrogenation over ZnZrO_x and Pd-ZnZrO_x catalysts was investigated. First, the apparent activation energy (E_a) of methanol formation was measured by using the Arrhenius plot (Fig. 4a). E_a is determined at 1.12 eV (108 kJ mol^{-1}) for undoped ZnZrO_x and gradually decreases as the Pd content increases (0.92 (88.8), 0.77 (74.3), and 0.69 (66.6) eV (kJ mol^{-1}) for 0.2%, 0.4%, and 0.8%Pd-ZnZrO_x, respectively). Notably, the reaction order of CO_2 is determined as 0.01–0.05 while the reaction order of H_2 is estimated as 0.94–1.00 for all catalysts (Fig. 4b and c). These values suggest that the concentration of surface-adsorbed CO_2 is high enough, but activating H_2 is related to the rate-determining step for ZnZrO_x and Pd-ZnZrO_x catalysts. Still, the atomically dispersed Pd species can promote the hydrogen activation, thereby increasing the rate of methanol formation.

It has been widely discussed that CO_2 dissociation to CO followed by CO hydrogenation is a plausible reaction pathway for metal-promoted In_2O_3 catalysts [45–48]. Thus, we further checked the CO hydrogenation activity of the catalysts. Compared to CO_2 hydrogenation, less than half methanol yield is observed under similar reaction conditions (Fig. S10). Further, the activity for CO hydrogenation to methanol gradually decreases as Pd content in catalyst increases. These results suggest that CO_2 is more active in methanol formation than CO on ZnZrO_x-based catalysts, and that the beneficial role of Pd promoter is likely not related to CO-mediated pathway.

To confirm the promoting effect of Pd on CO_2 hydrogenation over ZnZrO_x, we prepared ZnZrO_x and Pd-ZnZrO_x catalysts using other precursors and compared their catalytic performance (Fig. S11). Regardless of the type of precursor, the prepared Pd-ZnZrO_x catalysts always exhibit higher methanol yield compared to the Pd-free counterparts. The result further strengthens the argument that Pd-doping is beneficial for promoting CO_2 hydrogenation over ZnZrO_x.

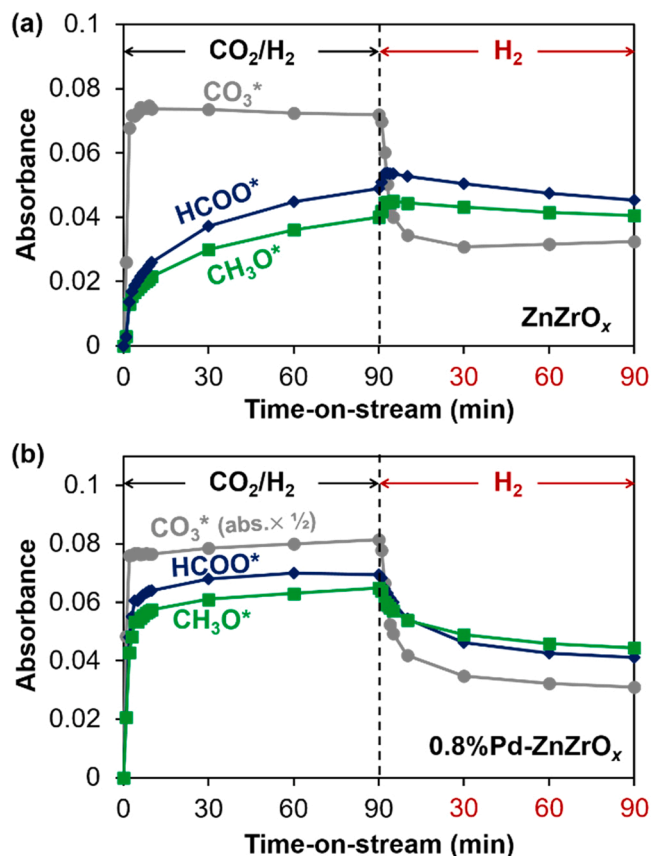


Fig. 6. Evolution of reaction intermediates recorded by *in situ* DRIFTS during CO_2 hydrogenation and sequential H_2 purging over (a) ZnZrO_x and (b) $0.8\%\text{Pd-ZnZrO}_x$. The peaks at 1525–1530, 2973–2978, 2933–2938 cm^{-1} were used for quantifying CO_3^* , HCOO^* , and CH_3O^* , respectively (Conditions: 523 K, 0.1 MPa, $\text{CO}_2/\text{H}_2 = 1:4$, $40 \text{ cm}^3 \text{ min}^{-1}$, and $W_{\text{cat}} = \text{ca. } 50 \text{ mg}$).

3.3. *In situ* DRIFTS analysis of Pd-ZnZrO_x under CO₂ and H₂

To gain additional insight into the superior CO_2 hydrogenation performance of Pd-ZnZrO_x compared to ZnZrO_x, we carried out *in situ* DRIFTS investigations. Spectra were collected at various temperatures (373–573 K) under CO_2/H_2 flow at ambient pressure (Fig. 5). They show that ZnZrO_x and $0.8\%\text{Pd-ZnZrO}_x$ catalysts bear similar surface species: CO_3^* (1528 cm^{-1}), HCOO^* (1366, 1586, 2735, 2878, and 2978 cm^{-1}), and CH_3O^* (1076, 2830, and 2936 cm^{-1}), where CO_3^* refers to adsorbed CO_2 bound with an oxygen atom in the catalyst lattice. HCOO^* and CH_3O^* are hydrogenated intermediate species. Earlier literature reported that HCOO^* (formate) formation followed by CH_3O^* (methoxide) generation is the most probable mechanism for methanol synthesis from CO_2 over ZnZrO_x and Cu-doped ZnZrO_x catalyst [26,49]. Our DRIFTS result suggests that Pd-ZnZrO_x also adopts a $\text{HCOO}^* \rightarrow \text{CH}_3\text{O}^*$ -mediated mechanism for methanol production. Meanwhile, linearly bound CO (CO^* , 2038 cm^{-1}) is only detected in the spectra of $0.8\%\text{Pd-ZnZrO}_x$ which reflects the feasible production of CO on Pd-ZnZrO_x catalysts. In the case of ZnZrO_x (Fig. 5a), the peak of hydrogenated species (e.g. HCOO^* and CH_3O^*) started to appear at 473 K and saturated around 523 K, confirming its high energy barrier for the hydrogenation step. The decreased intensity at 573 K is attributed to dominant desorption of surface intermediates. Notably, $0.8\%\text{Pd-ZnZrO}_x$ shows intense signals of HCOO^* and CH_3O^* even at a low temperature (e.g. 373 K), indicating a much lower energy barrier for hydrogenation on the Pd-promoted surface (Fig. 5b).

The evolution of surface species was also analyzed by monitoring the spectra changes over time-on-stream under the CO_2/H_2 flow for each

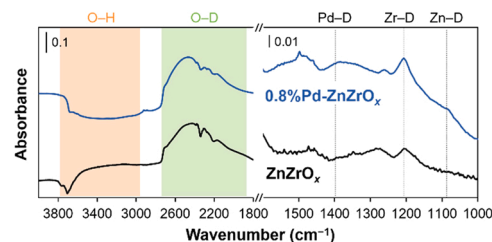


Fig. 7. D_2 -adsorbed DRIFT spectra of ZnZrO_x and $0.8\%\text{Pd-ZnZrO}_x$ catalysts at 323 K.

catalyst at 523 K—a condition that leads to the most intense peaks (Fig. S12). The changes of adsorbed species over time-on-stream are summarized in Fig. 6. For both ZnZrO_x and $0.8\%\text{Pd-ZnZrO}_x$ catalysts, the surface concentration of CO_3^* reached equilibrium under CO_2/H_2 flow very quickly, confirming that CO_2 adsorption is not the rate-determining step. On both catalysts, the surface concentration of HCOO^* and CH_3O^* changes simultaneously, thus we speculate that the concentration of HCOO^* is the key factor determining the overall reaction rate on both catalysts. For the ZnZrO_x catalyst, it took longer ($\geq 90 \text{ min}$) for the surface concentration of hydrogenated intermediates (HCOO^* and CH_3O^*) to reach the equilibrium state (Fig. 6a). On the other hand, the hydrogenated intermediates on $0.8\%\text{Pd-ZnZrO}_x$ saturated within ca. 10 min (Fig. 6b). This means that atomically dispersed Pd accelerates the formation of key hydrogenated intermediates (e.g. HCOO^*). After 90 min monitoring under CO_2/H_2 flow, the gas was switched to pure H_2 flow to follow the changes of surface-adsorbed species. On ZnZrO_x catalyst, CO_3^* diminishes immediately, whereas HCOO^* and CH_3O^* increase during the initial period (ca. 3 min) of the pure H_2 flow (Fig. 6a). This means the formation of HCOO^* and CH_3O^* from CO_3^* requires an excess amount of H_2 due to the poor H_2 activation capability of ZnZrO_x . After 3 min under H_2 flow, HCOO^* and CH_3O^* started to decrease very slowly. In contrast, HCOO^* and CH_3O^* on $0.8\%\text{Pd-ZnZrO}_x$ immediately decreased their intensity when gas was switched to pure H_2 (Fig. 6b). These results demonstrate that HCOO^* adsorbed on Pd-decorated surface is more reactive during hydrogenation.

To add more insights into the H_2 activation process on catalyst surface, we conducted D_2 -DRIFTS analysis. Both spectra for ZnZrO_x and $0.8\%\text{Pd-ZnZrO}_x$ show a decrease in O–H vibration alongside simultaneous increase in O–D vibration (Fig. 7), indicating surface –OH groups are changed to –OD during D_2 treatment. At the same time, the M–D vibrations were identified at 1400, 1205, 1087 cm^{-1} for M = Pd, Zr, Zn, respectively (the wavenumber of Zr–D vibration was estimated using the wavenumber of Zr–H vibration and reduced mass of oscillator) [60–62]. These observations evidence the heterolytic D_2 splitting (D^+ on oxygen anion and D^- on metal cation) on the ZnZrO_x surface. As expected, Pd–D is only observed on $0.8\%\text{Pd-ZnZrO}_x$, but Zn–D is also more pronounced on $0.8\%\text{Pd-ZnZrO}_x$, demonstrating a beneficial role of atomic Pd on hydrogen activation.

3.4. Simulations of the catalyst structure and promoting effect on CO₂ hydrogenation

DFT analysis of $\text{Pd}_1\text{-ZnZrO}_x$ provided more detailed information about its structure and the promoting mechanism of Pd during CO_2 hydrogenation. The model structure of ZnZrO_x solid solution was designed based on $t\text{-ZrO}_2$ crystal, where a Zn atom substitutes one of lattice Zr atoms at the surface. In line with the previous study on ZnZrO_x , our simulations revealed that Zn doping of the ZrO_2 surface generates one O-vacancy per unit cell with a Gibbs energy for the generation of an oxygen vacancy ($G_{\text{O-vac}}$) of -3.87 eV at the reaction conditions, which enables a +2-charge on the Zn atom [26,63]. $G_{\text{O-vac}}$ values for the generation of a second O-vacancy were calculated to be endothermic by

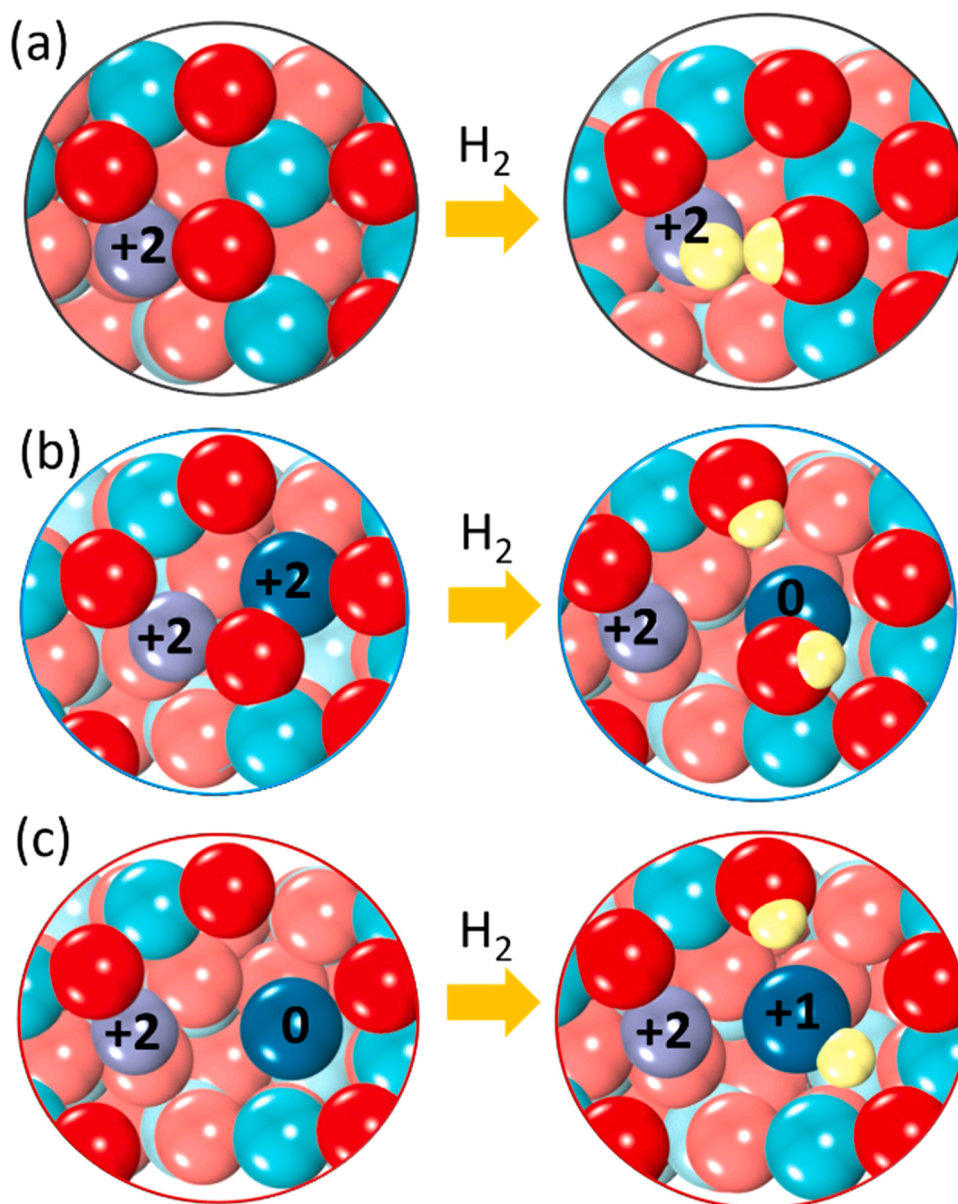


Fig. 8. Diagram showing surface O-vacancies and H-adsorption on (a) ZnZrO_x , (b) $\text{Pd}_1^{1+}\text{-ZnZrO}_x$ converted to $\text{Pd}_1^0\text{-ZnZrO}_x$ upon H_2 adsorption, and (c) $\text{Pd}_1^0\text{-ZnZrO}_x$ converted to $\text{Pd}_1^{1+}\text{-ZnZrO}_x$ upon H_2 adsorption. Bader charges on bare and H adsorbed catalyst surfaces are also provided. Red, turquoise, purple, cyan, and yellow colors represent O, Zr, Zn, Pd, and H, respectively. The top surface atoms are highlighted with more vivid colors.

at least 1.56 eV as shown in Fig. S13 for all possible O-sites near the Zn atom.

As Pd is atomically dispersed in ZnZrO_x and mostly keeps its highly dispersed nature during reaction, we consider that Pd has replaced lattice Zn or Zr atoms on the catalyst surface. In order to investigate the most plausible structure of $\text{Pd}_1\text{-ZnZrO}_x$, the $G_{\text{O-vac}}$ was calculated for various numbers and locations of oxygen vacancies (Fig. S14). As shown in Fig. S14a, the $G_{\text{O-vac}}$ for the first oxygen vacancy generation from fully crystalline structure is highly negative (−3.93 to −2.98 eV) for all oxygen atoms near Pd and Zn, which means that the first oxygen vacancy is prone to be generated at the most stable position adjacent to the Zn atom. Similarly, all oxygen positions have negative $G_{\text{O-vac}}$ (−2.21 to −0.22 eV) for the generation of the second oxygen vacancy (Fig. S14b) with the highest exothermicity exhibited by the site adjacent to Pd. Thus, in line with the XPS results (Fig. 2a and Table 1), Pd-doping significantly increases the number of surface O-vacancies, which are active sites for CO_2 hydrogenation. Bader charge analysis shows that the

charge on Zn atom remains constant irrespective of the number of vacancies per unit cell of the Pd-doped ZnZrO_x surface, which is in line with our XPS results (Fig. S4). However, the Pd atom is reduced with the formation of second vacancy to a Pd^{2+} charge state (Table S3).

In turn, further ex-situ reduction of Pd^{2+} to Pd^0 through the generation of the third oxygen vacancy is thermodynamically hindered (Fig. S14c). The least endothermic oxygen formation energy amounts to 0.17 eV under reaction conditions corresponding to the bridge position between Pd and Zn dopants. To analyze the thermodynamic stability of the proposed model in more detail, we calculated the phase diagram of Pd_1 -doped ZnZrO_x as a function of temperature and H_2 pressure in the reaction (Fig. S15). The results reveal that the reduction of Pd^{2+} to Pd^0 may be feasible at elevated temperatures and H_2 pressures in the system, which is consistent with the XANES result showing that Pd dopants exist in a mixture of 0 and +2 charge states (Fig. 1d and S8b).

Based on our experimental findings, we envision the possible reaction network on $\text{Pd}_1\text{-ZnZrO}_x$ catalyst as follows: 1) dissociative

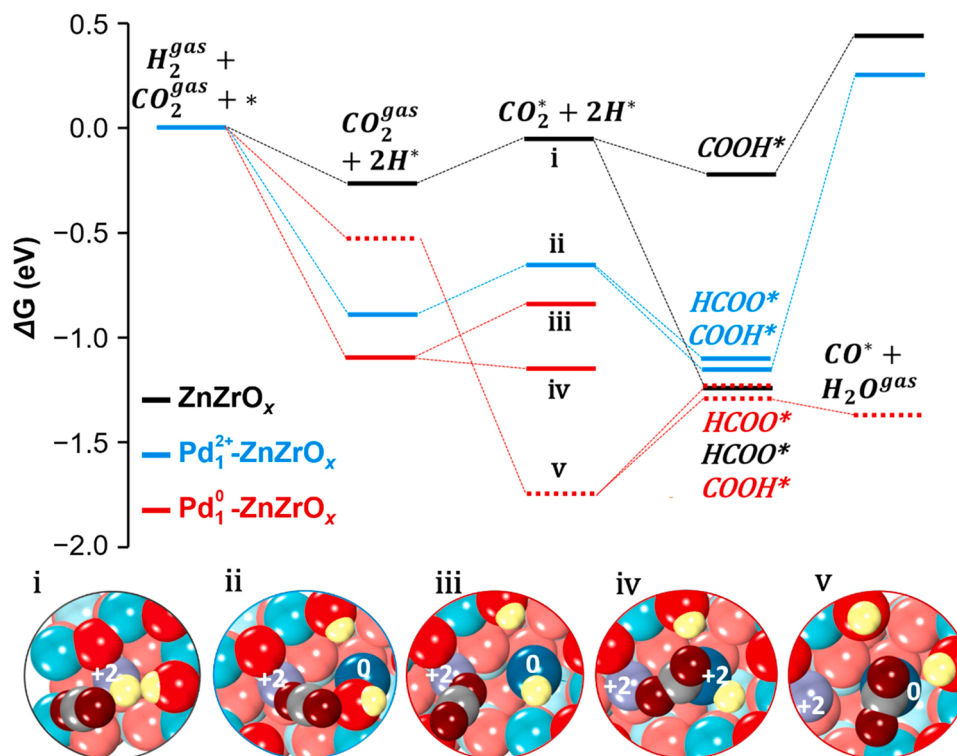


Fig. 9. Gibbs free energy reaction profile of HCOO* and CO* formation on the ZnZrO_x (black line), (Pd²⁺→Pd⁰)₁-ZnZrO_x (blue line), and (Pd⁰→Pd¹⁺)₁-ZnZrO_x (red line) surfaces. (Red, turquoise, purple, cyan, grey, and yellow colors represent O, Zr, Zn, Pd, C, and H, respectively. The top surface atoms are highlighted with more vivid colors.).

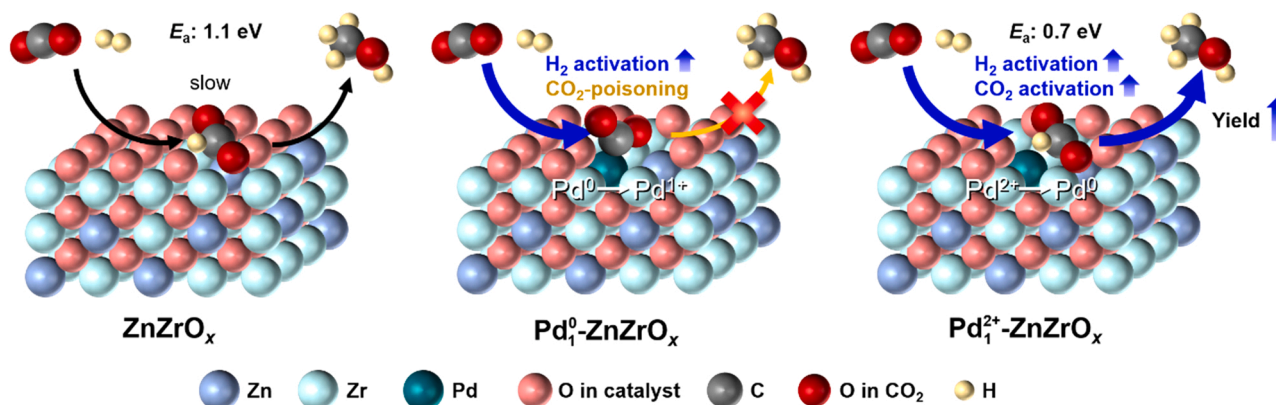
adsorption of H₂, 2) CO₂ adsorption on oxygen vacancies formed on the catalyst surface due to Pd and Zn-doping, 3) hydrogenation of adsorbed CO₂* to either HCOO* or COOH* intermediates, and further 4) COOH* hydrogenation to CO* and H₂O to finally predict the reaction mechanism pathway between HCOO* versus CO* for methanol synthesis. Since the cleavage of the H-C bond in the formed HCOO* is highly unlikely under hydrogenation conditions, many studies of methanol production catalysts concluded that further hydrogenation of HCOO*-eventually leads to methanol production,[26,49,64,65] which is also in line with the *in situ* DRIFTS results (Figs. 5–6). In turn, the COOH* intermediate can be further hydrogenated to either gaseous CO or to methanol, which depends on the relative kinetics of various elementary steps. Hereon, we briefly outline how density functional simulations shed light on each of these critical elementary steps for methanol synthesis.

First, the Gibbs free energy changes for all possible positions of dissociative adsorption of H₂ (Fig. S16) and the charges on Pd and Zn atoms upon O-vacancy formation and dissociated H adsorption (Fig. 8a–c) were screened in all the cases. On the ZnZrO_x surface (Fig. 8a), H₂ splitting results in the formation of H^{δ-} on the Zn atom and H^{δ+} on the lattice oxygen atom in the same surface positions as suggested by Wang et al. [26]. Bader charge analysis reveals that the charge on Zn atoms does not change even after hydrogenation of ZnZrO_x surface (Fig. 8a). However, on the Pd₁-ZnZrO_x surface, our calculations show that H₂ dissociation occurs in different ways depending on the charge on Pd (Fig. 8b–c). For example, heterolytic H₂ splitting is favored on Pd⁰-enriched surface. In this case, two hydrogen atoms bind to lattice O and Pd atoms which are oxidized from Pd⁰ to Pd¹⁺ (Fig. 8c). Similarly, when a Pd²⁺ atom is present on the surface, only H^{δ+} species are generated during H₂ dissociation, which also reduces +2 charge to 0 on Pd atom (Fig. 8b). Most importantly, Pd²⁺ and Pd⁰ dopants significantly facilitate H₂ activation, which becomes more exothermic by 0.9 eV than on the pristine ZnZrO_x surface (Fig. 9).

Second, the chemisorption of CO₂ was systematically investigated on

various possible sites of pristine and Pd₁-ZnZrO_x catalysts (Fig. S17). Gaseous CO₂ linearly adsorbs on the oxygen vacancy near the Zn atom on the ZnZrO_x surface with an energy change of −0.20 eV (Fig. S17a). Similarly, Pd₁-ZnZrO_x also acquire the same mode of CO₂ linear binding with the similar energies of ∼ −0.16 eV near Zn atom on both Pd²⁺ (converted *in situ* to Pd⁰; Fig. S17b) and Pd⁰ (converted *in situ* to Pd¹⁺; Fig. S17c). This finding is in line with the similar CO₂ desorption fingerprints on ZnZrO_x with and without Pd doping (Fig. 2c). Also, on ZnZrO_x doped by Pd⁰ (converted *in situ* to Pd¹⁺ upon H₂ adsorption), CO₂ may chemisorb in a bent configuration with an O-C-O angle of 130.3° in which C binds to Pd and O can bind to Zn or Zr depending on the location of CO₂ (Fig. S17d and e). The strongest CO₂ adsorption is calculated when C binds to Pd and O to Zr atom (*E*_{ads} = −1.89 eV) and H-atom adsorbed on Pd moves to adjacent oxygen to forms H^{δ+} surface species which changes the charge on Pd from +1 back to 0 (Fig. S17e).

Finally, Gibbs free energy profiles for the CO₂ hydrogenation to HCOO* and CO* intermediates on ZnZrO_x, Pd²⁺ and Pd⁰-doped surfaces were investigated (Fig. 9). Reaction energy profiles are based on the most stable positions of chemisorbed H*, CO₂*, HCOO*, COOH*, and CO* intermediates identified via systematic screening (Figs. S16–S22). HCOO* and COOH* bind to the surface metal cations in a bidentate fashion is the thermodynamically most favored adsorption configurations on ZnZrO_x and Pd-ZnZrO_x surfaces. The most exothermic reaction pathway on pristine ZnZrO_x is HCOO* formation using H adsorbed on Zn atom wherein the formation energy of the COOH* is less exothermic by 1.14 eV compared to HCOO*. On the other hand, CO₂ hydrogenation to both HCOO* and COOH* is similarly exothermic on Pd²⁺-ZnZrO_x which opens the possibility of both methanol and CO formation on this surface. Thus, to further investigate the plausible mechanism of methanol generation via CO* formation from COOH*, a systematic analysis of the most stable position of CO adsorption was conducted on all the catalysts surfaces (Fig. S22). CO was calculated to strongly bind (−2.37 eV) only to the Pd atom on fully reduced Pd⁰-ZnZrO_x, which



Scheme 1. Illustration of the effects of atomically dispersed Pd promoter on ZnZrO_x for CO₂ hydrogenation to methanol.

were calculated to be less thermodynamically stable and more prone to the poisoning by strongly bound CO₂ molecules than Pd₁²⁺-ZnZrO_x. In turn, weakly bounded CO on Zn or Zr atoms can easily desorb from the surface without further hydrogenation to other intermediates. Also, CO* formation from COOH* on partially reduced Pd₁²⁺-ZnZrO_x surface was calculated to be a highly endothermic reaction (1.37 eV), which will limit its extent. Finally, Pd⁰ dopants on ZnZrO_x are calculated to chemisorb CO₂ molecules with excessive strength that makes their further hydrogenation into HCOO* or COOH* endothermic by 0.45 eV and 0.47 eV, respectively (Fig. 9). The reaction energy profile without Gibbs energy corrections is included in the supporting information (Fig. S23).

Thus, the simulations overall reveal that atomically dispersed Pd in ZnZrO_x significantly increases the number of oxygen vacancies on the surface of the catalyst and also promotes dissociative adsorption of H₂ molecules, which was measured to be one of the key factors controlling the overall reaction rate. On the pristine ZnZrO_x, a highly exothermic CO₂ reduction produces HCOO*, the further hydrogenation of which leads to methanol production. Whereas Pd⁰ dopants are calculated to effectively be poisoned by strongly chemisorbed CO₂ molecules, the ZnZrO_x surface doped with Pd²⁺ is able to reduce CO₂ to both HCOO* and COOH* intermediates, whereas further hydrogenation of COOH* to CO* remains highly endothermic. Finally, we could compromise the effects of atomic Pd promoter for CO₂ hydrogenation to methanol from holistic experimental observations and theoretical analyses (Scheme 1). Methanol synthesis takes place via HCOO*-mediated mechanism on both ZnZrO_x and Pd₁-ZnZrO_x. The overall reaction rate highly depends on the surface coverage of HCOO*. Bare ZnZrO_x has poor H₂ activation ability, thus it has poor HCOO* formation/reaction activity which retard the overall reaction kinetics. Atomic Pd dopant can greatly accelerate H₂ activation regardless of the charge of Pd, therefore accelerating the overall reaction kinetics (*i.e.* E_a decreases to half) and significantly improving methanol yield. However, Pd₁⁰ (which becomes Pd₁⁺ after H₂ activation) is prone to be poisoned by too strong CO₂ binding, thus it is not effective for methanol synthesis.

4. Conclusions

We report an atomic Pd-promoted ZnZrO_x solid solution catalyst for CO₂ hydrogenation to methanol. A series of characterizations indicated that Pd-ZnZrO_x prepared by coprecipitation has atomically dispersed Pd species, which replace lattice Zn or Zr atoms on the surface up to 0.8 at% (*i.e.* 0.6 wt%). The atomic Pd-doping did not significantly alter textural properties of ZnZrO_x, but generated more surface oxygen vacancies, thus increasing the CO₂ adsorption capacity. Pd-doping in ZnZrO_x accelerated methanol formation rate, which was further enhanced during 100 h on stream test. Kinetic analyses and *in situ* DRIFTS revealed that the overall reaction rate could be determined by the surface concentration

of formate (HCOO*). Pd incorporation onto ZnZrO_x facilitates H₂ activation and the consequent formation of surface-formate, therefore sharply reducing the activation energy. DFT study supported that atomic Pd facilitates H₂ activation on the catalyst surface, which is transferred to adjacent Zn sites to accelerate the selective CO₂ hydrogenation. Overall, this work provides an atomic-level understanding of the structure and catalytic role of atomically dispersed metal catalyst for CO₂ hydrogenation, and may endow more opportunities for the development of efficient CO₂ valorization catalytic systems.

CRediT authorship contribution statement

Ning Yan supervised the project and revised the manuscript. Javier Pérez-Ramírez and Sergey M. Kozlov co-supervised the project and revised the manuscript. Kyungho Lee carried out most experiments, conducted data analysis and drafted the manuscript. Uzma Anjum conducted DFT calculations and drafted DFT related part. Qian He carried out STEM analysis. Shinya Furukawa was responsible for X-ray absorption analysis. All authors contributed to discussion of the work.

Declaration of Competing Interest

The authors declare that they have no known competing financial interests or personal relationships that could have appeared to influence the work reported in this paper.

Acknowledgements

This work was supported by the National University of Singapore Flagship Green Energy Programme (R-279-000-553-646). Computational work was performed using resources of the National Supercomputing Centre, Singapore. Q. He would like to acknowledge the support of the National Research Foundation (NRF) Singapore, under its NRF Fellowship (NRF-NRFF11-2019-0002). We thank Prof. Jishan Wu and Dr. Xudong Hou for conducting EPR analysis.

Appendix A. Supporting information

Supplementary data associated with this article can be found in the online version at [doi:10.1016/j.apcatb.2021.120994](https://doi.org/10.1016/j.apcatb.2021.120994).

References

- [1] T.R. Karl, K.E. Trenberth, Modern global climate change, *Science* 302 (2003) 1719–1723, <https://doi.org/10.1126/science.1090228>.
- [2] S.C. Doney, V.J. Fabry, R.A. Feely, J.A. Kleypas, Ocean acidification: the other CO₂ problem, *Annu. Rev. Mar. Sci.* 1 (2009) 169–192, <https://doi.org/10.1146/annurev.marine.010908.163834>.
- [3] G.A. Olah, Beyond oil and gas: the methanol economy, *Angew. Chem. Int. Ed.* 44 (2005) 2636–2639, <https://doi.org/10.1002/anie.200462121>.

- [4] F. Dalena, A. Senatore, A. Marino, A. Gordano, M. Basile, A. Basile, Methanol production and applications: an overview, *Methanol* (2018) 3–28, <https://doi.org/10.1016/B978-0-444-63903-5.00001-7>.
- [5] P. Gao, S. Li, X. Bu, S. Dang, Z. Liu, H. Wang, L. Zhong, M. Qiu, C. Yang, J. Cai, W. Wei, Y. Sun, Direct conversion of CO₂ into liquid fuels with high selectivity over a bifunctional catalyst, *Nat. Chem.* 9 (2017) 1019–1024, <https://doi.org/10.1038/nchem.2794>.
- [6] Y. Ni, Z. Chen, Y. Fu, Y. Liu, W. Zhu, Z. Liu, Selective conversion of CO₂ and H₂ into aromatics, *Nat. Commun.* 9 (2018) 3457, <https://doi.org/10.1038/s41467-018-05880-4>.
- [7] Y. Wang, L. Tan, M. Tan, P. Zhang, Y. Fang, Y. Yoneyama, G. Yang, N. Tsubaki, Rationally designing bifunctional catalysts as an efficient strategy to boost CO₂ hydrogenation producing value-added aromatics, *ACS Catal.* 9 (2019) 895–901, <https://doi.org/10.1021/acscatal.8b01344>.
- [8] Z. Li, Y. Qu, J. Wang, H. Liu, M. Li, S. Miao, C. Li, Highly selective conversion of carbon dioxide to aromatics over tandem catalysts, *Joule* 3 (2019) 570–583, <https://doi.org/10.1016/j.joule.2018.10.027>.
- [9] Z. Li, J. Wang, Y. Qu, H. Liu, C. Tang, S. Miao, Z. Feng, H. An, C. Li, Highly selective conversion of carbon dioxide to lower olefins, *ACS Catal.* 7 (2017) 8544–8548, <https://doi.org/10.1021/acscatal.7b03251>.
- [10] P. Gao, S. Dang, S. Li, X. Bu, Z. Liu, M. Qiu, C. Yang, H. Wang, L. Zhong, Y. Han, Q. Liu, W. Wei, Y. Sun, Direct production of lower olefins from CO₂ conversion via bifunctional catalysis, *ACS Catal.* 8 (2018) 571–578, <https://doi.org/10.1021/acscatal.7b02649>.
- [11] X. Liu, M. Wang, C. Zhou, W. Zhou, K. Cheng, J. Kang, Q. Zhang, W. Deng, Y. Wang, Selective transformation of carbon dioxide into lower olefins with a bifunctional catalyst composed of ZnGa₂O₄ and SAPO-34, *Chem. Commun.* 54 (2018) 140–143, <https://doi.org/10.1039/c7cc08642c>.
- [12] W. Wang, S. Wang, X. Ma, J. Gong, Recent advances in catalytic hydrogenation of carbon dioxide, *Chem. Soc. Rev.* 40 (2011) 3703–3727, <https://doi.org/10.1039/c1cs15008a>.
- [13] J. Graciani, K. Mudiyansele, F. Xu, A.E. Baber, J. Evans, S.D. Senanayake, D. J. Stacchiola, P. Liu, J. Hrbeek, J.F. Sanz, J.A. Rodriguez, Highly active copper-ceria and copper-ceria-titania catalysts for methanol synthesis from CO₂, *Science* 345 (2014) 546–550, <https://doi.org/10.1126/science.1253057>.
- [14] J.T. Sun, I.S. Metcalfe, M. Sahibzada, Deactivation of Cu/ZnO/Al₂O₃ methanol synthesis catalyst by sintering, *Ind. Eng. Chem. Res.* 38 (1999) 3868–3872, <https://doi.org/10.1021/ie990078s>.
- [15] M.V. Twigg, M.S. Spencer, Deactivation of copper metal catalysts for methanol decomposition, methanol steam reforming and methanol synthesis, *Top. Catal.* 22 (2003) 191–203, <https://doi.org/10.1023/A:1023567718303>.
- [16] M.B. Fichtl, D. Schlereth, N. Jacobsen, I. Kasatkin, J. Schumann, M. Behrens, R. Schlögl, O. Hinrichsen, Kinetics of deactivation on Cu/ZnO/Al₂O₃ methanol synthesis catalysts, *Appl. Catal. A: Gen.* 502 (2015) 262–270, <https://doi.org/10.1016/j.apcata.2015.06.014>.
- [17] J. Ye, C. Liu, D. Mei, Q. Ge, Active oxygen vacancy site for methanol synthesis from CO₂ hydrogenation on In₂O₃(110): a DFT study, *ACS Catal.* 3 (2013) 1296–1306, <https://doi.org/10.1021/cs400132a>.
- [18] O. Martin, A.J. Martin, C. Mondelli, S. Mitchell, T.F. Segawa, R. Hauert, C. Drouilly, D. Curulla-Ferré, J. Pérez-Ramírez, Indium oxide as a superior catalyst for methanol synthesis by CO₂ hydrogenation, *Angew. Chem. Int. Ed.* 55 (2016) 6261–6265, <https://doi.org/10.1002/anie.201600943>.
- [19] S. Dang, B. Qin, Y. Yang, H. Wang, J. Cai, Y. Han, S. Li, P. Gao, Y. Sun, Rationally designed indium oxide catalysts for CO₂ hydrogenation to methanol with high activity and selectivity, *Sci. Adv.* 6 (2020), <https://doi.org/10.1126/sciadv.aaz2060>.
- [20] M.S. Frei, C. Mondelli, A. Cesarini, F. Krumeich, R. Hauert, J.A. Stewart, D. Curulla Ferré, J. Pérez-Ramírez, Role of zirconia in indium oxide-catalyzed CO₂ hydrogenation to methanol, *ACS Catal.* 10 (2020) 1133–1145, <https://doi.org/10.1021/acscatal.9b03305>.
- [21] X. Jiang, X. Nie, Y. Gong, C.M. Moran, J. Wang, J. Zhu, H. Chang, X. Guo, K. S. Walton, C. Song, A combined experimental and DFT study of H₂O effect on In₂O₃/ZrO₂ catalyst for CO₂ hydrogenation to methanol, *J. Catal.* 383 (2020) 283–296, <https://doi.org/10.1016/j.jcat.2020.01.014>.
- [22] C. Yang, C. Pei, R. Luo, S. Liu, Y. Wang, Z. Wang, Z.J. Zhao, J. Gong, Strong electronic oxide-support interaction over In₂O₃/ZrO₂ for highly selective CO₂ hydrogenation to methanol, *J. Am. Chem. Soc.* 142 (2020) 19523–19531, <https://doi.org/10.1021/jacs.0c07195>.
- [23] A. Cao, Z. Wang, H. Li, J.K. Nørskov, Relations between surface oxygen vacancies and activity of methanol formation from CO₂ hydrogenation over In₂O₃ surfaces, *ACS Catal.* 11 (2021) 1780–1786, <https://doi.org/10.1021/acscatal.0c05046>.
- [24] J. Wang, G. Zhang, J. Zhu, X. Zhang, F. Ding, A. Zhang, X. Guo, C. Song, CO₂ hydrogenation to methanol over In₂O₃-based catalysts: from mechanism to catalyst development, *ACS Catal.* 11 (2021) 1406–1423, <https://doi.org/10.1021/acscatal.0c03665>.
- [25] A. Tsoulalou, P.M. Abdala, A. Armutlulu, E. Willinger, A. Fedorov, C.R. Müller, Operando X-ray absorption spectroscopy identifies a monoclinic ZrO₂ in solid solution as the active phase for the hydrogenation of CO to methanol, *ACS Catal.* 10 (2020) 10060–10067, <https://doi.org/10.1021/acscatal.0c01968>.
- [26] J. Wang, G. Li, Z. Li, C. Tang, Z. Feng, H. An, H. Liu, T. Liu, C. Li, A highly selective and stable ZnO-ZrO₂ solid solution catalyst for CO₂ hydrogenation to methanol, *Sci. Adv.* 3 (2017), e1701290, <https://doi.org/10.1126/sciadv.1701290>.
- [27] J. Wang, C. Tang, G. Li, Z. Han, Z. Li, H. Liu, F. Cheng, C. Li, High-performance MaZrOx (Ma = Cd, Ga) solid-solution catalysts for CO₂ hydrogenation to methanol, *ACS Catal.* 9 (2019) 10253–10259, <https://doi.org/10.1021/acscatal.9b03449>.
- [28] W. Li, K. Wang, J. Huang, X. Liu, D. Fu, J. Huang, Q. Li, G. Zhan, M_xO_y-ZrO₂ (M = Zn, Co, Cu) solid solutions derived from schiff base-bridged UiO-66 composites as high-performance catalysts for CO₂ hydrogenation, *ACS Appl. Mater. Interfaces* 11 (2019) 33263–33272, <https://doi.org/10.1021/acsami.9b11547>.
- [29] Z. Han, C. Tang, F. Sha, S. Tang, J. Wang, C. Li, CO₂ hydrogenation to methanol on ZnO-ZrO₂ solid solution catalysts with ordered mesoporous structure, *J. Catal.* 396 (2021) 242–250, <https://doi.org/10.1016/j.jcat.2021.02.024>.
- [30] X. Fang, Y. Xi, H. Jia, C. Chen, Y. Wang, Y. Song, T. Du, Tetragonal zirconia based ternary ZnO-ZrO₂-MO_x solid solution catalysts for highly selective conversion of CO₂ to methanol at high reaction temperature, *J. Ind. Eng. Chem.* 88 (2020) 268–277, <https://doi.org/10.1016/j.jiec.2020.04.024>.
- [31] S. Zhou, S. Li, Insights into the high activity and methanol selectivity of the Zn/ZrO₂ solid solution catalyst for CO₂ hydrogenation, *J. Phys. Chem. C* 124 (2020) 27467–27478, <https://doi.org/10.1021/acs.jpcc.0c07433>.
- [32] J. Qu, X. Zhou, F. Xu, X.-Q. Gong, S.C.E. Tsang, Shape effect of Pd-promoted Ga₂O₃ nanocatalysts for methanol synthesis by CO₂ hydrogenation, *J. Phys. Chem. C* 118 (2014) 24452–24466, <https://doi.org/10.1021/jp5063379>.
- [33] F. Jiang, S. Wang, B. Liu, J. Liu, L. Wang, Y. Xiao, Y. Xu, X. Liu, Insights into the influence of CeO₂ crystal facet on CO₂ hydrogenation to methanol over Pd/CeO₂ catalysts, *ACS Catal.* 10 (2020) 11493–11509, <https://doi.org/10.1021/acscatal.0c03324>.
- [34] N. Rui, Z. Wang, K. Sun, J. Ye, Q. Ge, C.-j. Liu, CO₂ hydrogenation to methanol over Pd/In₂O₃: effects of Pd and oxygen vacancy, *Appl. Catal. B Environ.* 218 (2017) 488–497, <https://doi.org/10.1016/j.apcatb.2017.06.069>.
- [35] M.S. Frei, C. Mondelli, R. García-Muelas, K.S. Kley, B. Puértolas, N. López, O. V. Safonova, J.A. Stewart, D. Curulla Ferré, J. Pérez-Ramírez, Atomic-scale engineering of indium oxide promotion by palladium for methanol production via CO₂ hydrogenation, *Nat. Commun.* 10 (2019) 3377, <https://doi.org/10.1038/s41467-019-11349-9>.
- [36] Z. Han, C. Tang, J. Wang, L. Li, C. Li, Atomically dispersed Pt⁺ species as highly active sites in Pt/In₂O₃ catalysts for methanol synthesis from CO₂ hydrogenation, *J. Catal.* 394 (2021) 236–244, <https://doi.org/10.1016/j.jcat.2020.06.018>.
- [37] N.H.M.D. Dostagir, C. Thompson, H. Kobayashi, A.M. Karim, A. Fukuoka, A. Shrotri, Rh promoted In₂O₃ as a highly active catalyst for CO₂ hydrogenation to methanol, *Catal. Sci. Technol.* 10 (2020) 8196–8202, <https://doi.org/10.1039/d0cy01789b>.
- [38] N. Rui, F. Zhang, K. Sun, Z. Liu, W. Xu, E. Stavitski, S.D. Senanayake, J. A. Rodriguez, C.-J. Liu, Hydrogenation of CO₂ to methanol on a Au⁺-In₂O_{3-x} catalyst, *ACS Catal.* 10 (2020) 11307–11317, <https://doi.org/10.1021/acscatal.0c02120>.
- [39] J.L. Snider, V. Streibel, M.A. Hubert, T.S. Choksi, E. Valle, D.C. Upham, J. Schumann, M.S. Dwyer, A. Gallo, F. Abild-Pedersen, T.F. Jaramillo, Revealing the synergy between oxide and alloy phases on the performance of bimetallic In-Pd catalysts for CO₂ hydrogenation to methanol, *ACS Catal.* 9 (2019) 3399–3412, <https://doi.org/10.1021/acscatal.8b04848>.
- [40] J. Zhu, F. Cannizzaro, L. Liu, H. Zhang, N. Kosinov, I.A.W. Filot, J. Rabeah, A. Brückner, E.J.M. Hensen, Ni-in synergy in CO₂ hydrogenation to methanol, *ACS Catal.* (2021) 11371–11384, <https://doi.org/10.1021/acscatal.1c03170>.
- [41] X. Yang, S. Kattel, S.D. Senanayake, J.A. Boscoboinik, X. Nie, J. Graciani, J. A. Rodriguez, P. Liu, D.J. Stacchiola, J.G. Chen, Low pressure CO₂ hydrogenation to methanol over gold nanoparticles activated on a CeO_x/TiO₂ interface, *J. Am. Chem. Soc.* 137 (2015) 10104–10107, <https://doi.org/10.1021/jacs.5b06150>.
- [42] X. Jia, K. Sun, J. Wang, C. Shen, C.-j. Liu, Selective hydrogenation of CO₂ to methanol over Ni/In₂O₃ catalyst, *J. Energy Chem.* 50 (2020) 409–415, <https://doi.org/10.1016/j.jechem.2020.03.083>.
- [43] M.M. Li, H. Zou, J. Zheng, T.S. Wu, T.S. Chan, Y.L. Soo, X.P. Wu, X.Q. Gong, T. Chen, K. Roy, G. Held, S.C.E. Tsang, Methanol synthesis at a wide range of H₂/CO₂ ratios over a Rh-in bimetallic catalyst, *Angew. Chem., Int. Ed.* 59 (2020) 16039–16046, <https://doi.org/10.1002/anie.202000841>.
- [44] M.S. Frei, C. Mondelli, R. García-Muelas, J. Morales-Vidal, M. Philipp, O. V. Safonova, N. López, J.A. Stewart, D.C. Ferre, J. Pérez-Ramírez, Nanostructure of nickel-promoted indium oxide catalysts drives selectivity in CO₂ hydrogenation, *Nat. Commun.* 12 (2021) 1960, <https://doi.org/10.1038/s41467-021-22224-x>.
- [45] C. Shen, K. Sun, Z. Zhang, N. Rui, X. Jia, D. Mei, C.-j. Liu, Highly active Ir/In₂O₃ catalysts for selective hydrogenation of CO₂ to methanol: experimental and theoretical studies, *ACS Catal.* 11 (2021) 4036–4046, <https://doi.org/10.1021/acscatal.0c05628>.
- [46] Q. Wu, C. Shen, N. Rui, K. Sun, C.-j. Liu, Experimental and theoretical studies of CO₂ hydrogenation to methanol on Ru/In₂O₃, *J. CO₂ Util.* 53 (2021), 101720, <https://doi.org/10.1016/j.jcou.2021.101720>.
- [47] K. Sun, N. Rui, C. Shen, C.-j. Liu, Theoretical study of selective hydrogenation of CO₂ to methanol over Pt₄/In₂O₃ model catalyst, *J. Phys. Chem. C* 125 (2021) 10926–10936, <https://doi.org/10.1021/acs.jpcc.1c00638>.
- [48] C. Shen, Q. Bao, W. Xue, K. Sun, Z. Zhang, X. Jia, D. Mei, C.-j. Liu, Synergistic effect of the metal-support interaction and interfacial oxygen vacancy for CO₂ hydrogenation to methanol over Ni/In₂O₃ catalyst: a theoretical study, *J. Energy Chem.* 65 (2022) 623–629.
- [49] D. Xu, X. Hong, G. Liu, Highly dispersed metal doping to ZnZr oxide catalyst for CO₂ hydrogenation to methanol: insight into hydrogen spillover, *J. Catal.* 393 (2021) 207–214, <https://doi.org/10.1016/j.jcat.2020.11.039>.
- [50] C. Huang, Z. Wu, H. Luo, S. Zhang, Z. Shao, H. Wang, Y. Sun, CO₂ hydrogenation to methanol over PdZnZr solid solution: effects of the PdZn alloy and oxygen vacancy, *ACS Appl. Energy Mater.* 4 (2021) 9258–9266, <https://doi.org/10.1021/acsaem.1c01502>.

- [51] G. Kresse, J. Furthmüller, Efficient iterative schemes for ab initio total-energy calculations using a plane-wave basis set, *Phys. Rev. B* 54 (1996) 11169, <https://doi.org/10.1103/PhysRevB.54.11169>.
- [52] G. Kresse, D. Joubert, From ultrasoft pseudopotentials to the projector augmented-wave method, *Phys. Rev. B* 59 (1999) 1758, <https://doi.org/10.1103/PhysRevB.59.1758>.
- [53] H.J. Monkhorst, J.D. Pack, Special points for Brillouin-zone integrations, *Phys. Rev. B* 13 (1976) 5188, <https://doi.org/10.1103/PhysRevB.13.5188>.
- [54] A.H. Larsen, J.J. Mortensen, J. Blomqvist, I.E. Castelli, R. Christensen, M. Dulak, J. Friis, M.N. Groves, B. Hammer, C. Hargus, The atomic simulation environment—a Python library for working with atoms, *J. Phys.: Condens. Matter* 29 (2017), 273002, <https://doi.org/10.1088/1361-648X/aa680e>.
- [55] C. Wang, G. Garbarino, L.F. Allard, F. Wilson, G. Busca, M. Flytzani-Stephanopoulos, Low-temperature dehydrogenation of ethanol on atomically dispersed gold supported on ZnZrO_x, *ACS Catal.* 6 (2016) 210–218, <https://doi.org/10.1021/acscatal.5b01593>.
- [56] C. Wang, M. Ouyang, M. Li, S. Lee, M. Flytzani-Stephanopoulos, Low-coordinated Pd catalysts supported on Zn₁Zr₁O_x composite oxides for selective methanol steam reforming, *Appl. Catal. A Gen.* 580 (2019) 81–92, <https://doi.org/10.1016/j.apcata.2019.05.006>.
- [57] P.M. Lenahan, J. Conley Jr, What can electron paramagnetic resonance tell us about the Si/SiO₂ system? *J. Vac. Sci. Technol. B* 16 (1998) 2134–2153, <https://doi.org/10.1116/1.590301>.
- [58] H. Liu, F. Zeng, Y. Lin, G. Wang, F. Pan, Correlation of oxygen vacancy variations to band gap changes in epitaxial ZnO thin films, *Appl. Phys. Lett.* 102 (2013), 181908, <https://doi.org/10.1063/1.4804613>.
- [59] T. Sayle, S. Parker, C. Catlow, The role of oxygen vacancies on ceria surfaces in the oxidation of carbon monoxide, *Surf. Sci.* 316 (1994) 329–336, [https://doi.org/10.1016/0039-6028\(94\)91225-4](https://doi.org/10.1016/0039-6028(94)91225-4).
- [60] L. Andrews, X. Wang, M.E. Alikhani, L. Manceron, Observed and calculated infrared spectra of Pd(H₂)_{1,2,3} complexes and palladium hydrides in solid argon and neon, *J. Phys. Chem. A* 105 (2001) 3052–3063, <https://doi.org/10.1021/jp003721t>.
- [61] J. Corker, F. Lefebvre, C. Lecuyer, V. Dufaud, F. Quignard, Agnes Choplin, J. Evans, J.-M. Basset, Catalytic cleavage of the C-H and C-C bonds of alkanes by surface organometallic chemistry: an EXAFS and IR characterization of a Zr-H catalyst, *Science* 271 (1996) 966–969, <https://doi.org/10.1126/science.271.5251.966>.
- [62] T.M. Greene, W. Brown, L. Andrews, A.J. Downs, G.V. Chertihin, N. Runeberg, P. Pytko, Matrix infrared spectroscopic and ab initio studies of ZnH₂, CdH₂, and related metal hydride species, *J. Phys. Chem.* 99 (1995) 7925–7934, <https://doi.org/10.1021/j100020a014>.
- [63] P. Ticali, D. Salusso, R. Ahmad, C. Ahoba-Sam, A. Ramirez, G. Shterk, K. A. Lomachenko, E. Borfecchia, S. Morandi, L. Cavallo, J. Gascon, S. Bordiga, U. Olsbye, CO₂ hydrogenation to methanol and hydrocarbons over bifunctional Zn-doped ZrO₂/zeolite catalysts, *Catal. Sci. Technol.* 11 (2021) 1249–1268, <https://doi.org/10.1039/d0cy01550d>.
- [64] S. Kattel, P.J. Ramírez, J.G. Chen, J.A. Rodriguez, P. Liu, Active sites for CO₂ hydrogenation to methanol on Cu/ZnO catalysts, *Science* 355 (2017) 1296–1299, <https://doi.org/10.1126/science.aal3573>.
- [65] K. Larmier, W.C. Liao, S. Tada, E. Lam, R. Verel, A. Bansode, A. Urakawa, A. Comas-Vives, C. Coperet, CO₂-to-methanol hydrogenation on zirconia-supported copper nanoparticles: reaction intermediates and the role of the metal-support interface, *Angew. Chem. Int. Ed.* 56 (2017) 2318–2323, <https://doi.org/10.1002/anie.201610166>.